THE JOURNAL OF PHYSICAL CHEMISTRY C

Article

pubs.acs.org/JPCC

Eu^{3+}-Doped Wide Band Gap Zn_2SnO_4 Semiconductor Nanoparticles: Structure and Luminescence

Mirjana Dimitrievska,*[†,‡,§] Tamara B. Ivetić,[⊥] Alexander P. Litvinchuk,[#] Andrew Fairbrother,[§] Bojan B. Miljević,[⊥,¶] Goran R. Štrbac,[⊥] Alejandro Pérez Rodríguez,[§,□] and Svetlana R. Lukić-Petrović[⊥]

[†]NIST Center for Neutron Research, National Institute of Standards and Technology, Gaithersburg, Maryland 20899-6102, United States

[‡]National Renewable Energy Laboratory (NREL), Golden, Colorado 80401, United States

[§]Catalonia Institute for Energy Research (IREC), Jardins de les Dones de Negre, 1, 08930 Sant Adrià de Besòs, Barcelona, Barcelona, Spain

[⊥]Department of Physics, University of Novi Sad, Faculty of Sciences, Trg Dositeja Obradovica 4, 21000 Novi Sad, Serbia

[#]Texas Center for Superconductivity and Department of Physics, University of Houston, Houston, Texas 77204-5002, United States

[¶]Faculty of Technology, Department of Materials Engineering, University of Novi Sad, Bul. cara Lazara 1, 21000 Novi Sad, Serbia

[□]IN2UB, Universitat de Barcelona, C. Martí Franquès 1, 08028 Barcelona, Spain

Supporting Information

ABSTRACT: Nanocrystalline Zn_2SnO_4 powders doped with Eu^{3+} ions were synthesized via a mechanochemical solid-state reaction method followed by postannealing in air at 1200 °C. X-ray diffraction (XRD), energy-dispersive X-ray (EDX), and Raman and photoluminescence (PL) spectroscopies provide convincing evidence for the incorporation of Eu^{3+} ions into the host matrix on non-centrosymmetric sites of the cubic inverse spinel lattice. Microstructural analysis shows that the crystalline grain size decreases with the addition of Eu^{3+}. Formation of a nanocrystalline $Eu_2Sn_2O_7$ secondary phase is also observed. Luminescence spectra of Eu^{3+}-doped samples show several emissions, including narrow-band magnetic dipole emission at 595 nm and electric dipole emission at 615 nm of the Eu^{3+} ions. Excitation spectra and lifetime measurements suggest that Eu^{3+} ions are incorporated at only one symmetry site. According to the crystal field theory, it is assumed that Eu^{3+} ions participate at octahedral sites of Zn^{2+} or Sn^{4+} under a weak crystal field, rather than at the tetrahedral sites of Zn^{2+}, because of the high octahedral stabilization energy for Eu^{3+}. Activation of symmetry forbidden (IR-active and silent) modes is observed in the Raman scattering spectra of both pure and doped samples, indicating a disorder of the cation sublattice of Zn_2SnO_4 nanocrystallites. These results were further supported by the first principle lattice dynamics calculations. The spinel-type Zn_2SnO_4 shows effectiveness in hosting Eu^{3+} ions, which could be used as a prospective green/red emitter. This work also illustrates how sustainable and simple preparation methods could be used for effective engineering of material properties.

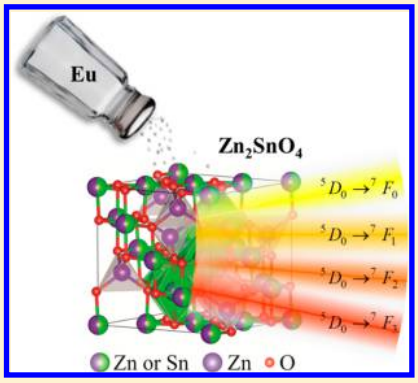

1. INTRODUCTION

Zinc stannate (Zn_2SnO_4) is a transparent n-type semiconducting oxide[1] with a diverse array of applications, such as in lead-free ferroelectrics, gas sensors, transparent conductors, lithium-ion batteries, dye-sensitized solar cells, and photocatalysis.[2] As a wide band gap material, it also has good potential for full color phosphors;[3] however, there are only a few reports on the possibility of Zn_2SnO_4 hosting an activator ion for this kind of application.[4,5] Among different possible dopants, the rare-earth ions including those of Eu, Tb, Er, Ce, Tm, Ho, and Nd are the most attractive because of their characteristic electronic transitions that could lead to sharp luminescence features in the ultraviolet (UV) to infrared (IR) range. Among rare-earth activator ions, europium stands out because it may exist in both divalent (Eu^{2+}) and trivalent (Eu^{3+}) states, each with very different emitting characteristics. The source for the Eu^{2+} ions is the reduction of $Eu^{3+} \rightarrow Eu^{2+}$ in a matrix if preparation is carried out in a reducing atmosphere or in some special compounds even in air at high temperatures.[6] The orange−red photoluminescence of Eu^{3+} originates from f−f transitions that are considered nearly independent of the host lattice, that is, emission from the $^5D_0$ state (595 nm: $^5D_0 \rightarrow {}^7F_1$; 610−620 nm: $^5D_0 \rightarrow {}^7F_2$).[7]

Mechanochemistry has a long history and has provided simple and sustainable production routes for functionally tailored nanomaterials.[8] The mechanically initiated chemical

Received: May 26, 2016
Revised: August 1, 2016
Published: August 3, 2016

DOI: 10.1021/acs.jpcc.6b05335
J. Phys. Chem. C 2016, 120, 18887−18894

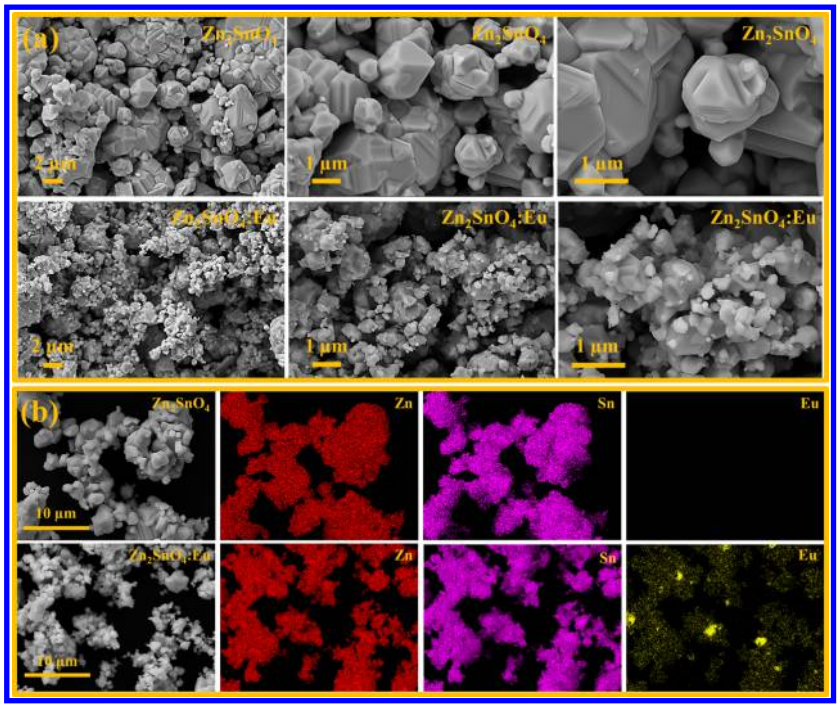

Figure 1. (a) SEM micrographs of Zn_2SnO_4 and Zn_2SnO_4:Eu nanoparticles at different magnifications. (b) EDX elemental mappings of the nanoparticles showing a uniform distribution of Zn and Sn for doped and undoped samples, with some regions of high Eu concentration in the doped sample.

reactions of oxides are typically accompanied by cation redistribution, formation of defect centers with unsaturated oxygen coordination, phase transformations, and so forth.

Here, this rather simple method of synthesis is employed to solve the comparatively complex and challenging task of nanocrystal doping. The structural and luminescence properties of mechanochemically synthesized Zn_2SnO_4 nanoparticles and the changes induced by europium doping were investigated experimentally, and the results are shown to compare favorably with those calculated within density functional theory.

2. EXPERIMENTAL DETAILS

Sample Preparation. Zn_2SnO_4 nanopowder was prepared via mechanochemical processing, in which starting precursors (ZnO and SnO_2, Sigma−Aldrich,[9] purity 99.9%, and particle size ≤ 1 μm) were mixed in stoichiometric quantities in a ball mill (Retsch GmbH PM100) using zirconia vial and zirconia balls of 10 mm diameter. A standard ball mass to powder mass ratio of 10:1 was used, followed by milling for 160 min (speed 320 rpm), after which the powder was subjected to an annealing step at 1200 °C for 120 min in an air atmosphere. The selection of these synthesis conditions was made on the basis of previous experimental results.[10] Europium-doped zinc stannate (Zn_2SnO_4:Eu) was prepared in a similar way, execept 1 at. % of Eu (Eu_2O_3, Aldrich, purity 99.99%) was added to the starting powder mixture.

Characterization. X-ray diffraction (XRD) analysis was used for structural characterization of zinc tin oxide samples and was carried out using a Philips PW 1050 diffractometer with Cu $K_{\alpha 1,2}$ radiation and a step scan mode of 0.02°/3s in the angular range of 2θ = 10−90°.

The morphology and microstructure of the obtained powder samples were investigated with scanning electron microscopy (SEM, Zeiss Series Auriga FE-SEM, operated at 10 kV)), and elemental mappings were made with an X-ray detector (energy-dispersive X-ray (EDX), Oxford Instruments X-Max) coupled directly to the SEM.

A detailed structural and vibrational analysis of the samples was performed using multiwavelength excitation Raman measurements combining ultraviolet (325 nm), blue (442 nm), green (532 nm), red (633 nm), and near-infrared (785 nm) excitation lines. Room temperature Raman scattering and photoluminescence (PL) measurements were performed in the back-scattering configuration with an iHR320 Horiba Jobin Yvon system combined with an Olympus metallographic microscope.[11,12] In all cases, the laser spot size diameter was about 1−2 μm, depending on the excitation wavelength. To avoid effects in the spectra related to potential microscopic inhomogeneities, the spot was rastered over an area of 30 × 30 μm^2 using a DuoScan accessory. The first-order Raman spectrum of monocrystalline Si was measured as a reference before and after acquisition of each Raman spectrum, and the spectra were corrected with respect to the Si line at 520 cm^{-1}. Spectral resolution was <2 cm^{-1} for all Raman measurements and <0.25 nm in the case of PL measurements performed with 532 nm excitation.

Additional luminescence excitation and emission spectra, as well as lifetime measurements, were obtained at room temperature using a Fluorolog-3 Model FL3-221 spectrofluorometer system (HORIBA Jobin-Yvon), incorporating a 450 W xenon lamp for emission measurements and a 150 W pulsed xenon lamp for lifetime measurements, while a HORIBA Jobin-Yvon TBX detector was utilized in both cases.

The diffuse reflectance spectra (DRS) were obtained using an Ocean Optics QE65000 high-sensitivity fiber optic spectrometer, and the optical band gap of the powders was estimated in accordance with the Kubelka−Munk function using SpectraSuite Ocean Optics operating software.

Theoretical Calculations. Density functional theory (DFT) calculations of the electronic ground state for

DOI: 10.1021/acs.jpcc.6b05335
J. Phys. Chem. C 2016, 120, 18887−18894

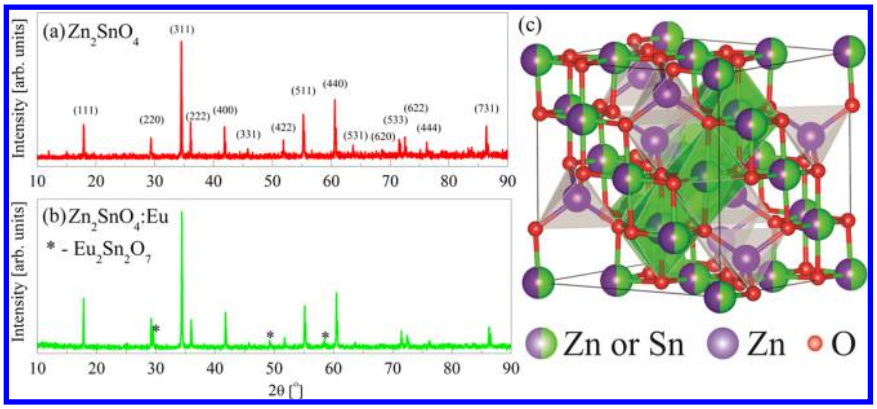

Figure 2. XRD patterns of (a) Zn_2SnO_4 and (b) Zn_2SnO_4:Eu nanoparticles. (c) The cubic inverse spinel structure of Zn_2SnO_4. Zn^{2+} and Sn^{4+} cations are distributed over the sites of tetrahedral and octahedral coordination. In the bulk material, one-half of Zn^{2+} ions occupy the sites of the tetrahedral coordination, whereas Sn^{4+} cations and the other half of Zn^{2+} ions occupy the sites of the octahedral coordination. Thus, the crystal chemical formula of Zn_2SnO_4, emphasizing the site occupancy at the atomic level, may be written as $(Zn^{2+})[Sn^{4+}Zn^{2+}]O_4$.

Zn_2SnO_4 of the cubic inverse spinel structure were performed within the generalized gradient approximation using the Perdew–Burke–Ernzerhof local functional[13] and norm-conserving pseudopotentials, as implemented in the CASTEP code.[14] The cutoff energy for the plane wave basis was set to 830 eV. Prior to performing calculations, internal atomic coordinates of oxygen were relaxed, so that forces on atoms in the equilibrium position did not exceed 1 meV $Å^{-1}$. A self-consistent field (SCF) tolerance better than 10^{-7} eV and the phonon SCF threshold of 10^{-12} eV were imposed. For calculations of the electronic structure and other relevant electronic properties, integration within the Brillouin zone of the primitive cell was performed over a 3 × 3 × 3 Monkhorst–Pack grid[15] in reciprocal space. Lattice vibration frequencies were further calculated by the finite displacement method.

All structural depictions were made using the VESTA (visualization for electronic and structural analysis) software.[16]

For all figures, standard uncertainties are commensurate with the observed scatter in the data, if not explicitly designated by vertical error bars.

3. RESULTS AND DISCUSSION

3.1. Morphology and Crystal Structure of Zn_2SnO_4 and Zn_2SnO_4:Eu Nanoparticles. Both the doped and undoped zinc stannate powders contain a nonuniform distribution of particle size and shape, as observed by SEM (Figure 1). This nonuniformity arises from the mechanical processing of the powders, while agglomeration of particles occurs during the high temperature annealing step. The undoped particles range from hundreds of nanometers up to a few micrometers or more in size, while the doped particles are noticeably smaller, commonly less than 100 nm in size, and rarely exceed 1 μm. This variation can be explained by differences in recrystallization energies: in general, the introduction of dopants increases the recrystallization energy, thus resulting in a smaller particle size for a given temperature. Large-area EDX measurements show Zn/Sn compositional ratios of 1.90 and 1.95 for the undoped and doped ZTO samples, respectively. Elemental mappings show a very uniform distribution of Zn and Sn in the particles, suggesting that Zn and Sn binary phases are not formed in spite of the slightly Sn-rich composition (confirmed next by XRD and Raman measurements). In the Eu-doped powder, the overall Eu concentration is 0.80 at. %, and there are areas with a high concentration of Eu, indicating the presence of a secondary phase ($Eu_2Sn_2O_7$, discussed further during XRD and Raman characterization). Outside of regions with this secondary phase, Eu is uniformly distributed along with Zn and Sn.

XRD analysis of the synthesized powders confirms the formation of a highly crystalline Zn_2SnO_4 phase in both cases (Figure 2a and b). XRD patterns agree very well with that of PDF (JCPDS 74–2184) for face-centered cubic inverse spinel Zn_2SnO_4 (space group $Fd\bar{3}m$ (O_h^7)). However, three impurity-related diffraction peaks in the XRD pattern of the Zn_2SnO_4:Eu sample were noticed and can be assigned to europium tin oxide ($Eu_2Sn_2O_7$, JCPDS 13–0182).

Zn_2SnO_4 crystallizes in the inverse spinel (B_2AO_4) structure, where tetrahedral sites are occupied by B atoms and the octahedral sites are occupied randomly by an equal number of A and B atoms.[17] Therefore, the structural formula of spinel-type zinc stannate may be written as $(Zn^{2+})[Sn^{4+}Zn^{2+}]O_4$ to denote that half of the Zn^{2+} cations are in sites of tetrahedral coordination and that the other half and all of the Sn^{4+} cations are in sites of octahedral coordination. The crystal structure obtained from the Rietveld refinement of the XRD pattern for the pure Zn_2SnO_4 compound is presented in Figure 2c.

An increase in the Zn_2SnO_4 lattice constant a (from 8.610(2) Å to 8.639(4) Å) for the Zn_2SnO_4:Eu system is observed, indicating that some europium ions have substituted the Zn^{2+} and Sn^{4+} sites in the Zn_2SnO_4 matrix. The observed local deformation in Zn_2SnO_4 lattice occurs because the substitution of smaller Zn^{2+} (0.74 Å) and Sn^{4+} (0.69 Å) ions with a larger size Eu^{3+} ion (0.95 Å) must lead to an increase in cell parameters and volume. Nevertheless, the significant difference in ionic radii between these cations makes extensive substitution difficult, so the formation of the secondary phase ($Eu_2Sn_2O_7$) is possible and even expected.[5]

Additionally, Williams–Hall (W–H) analysis[17−19] was performed in order to determine and compare the average nanocrystallite size and the microstrain in these materials. The results show that the average domain size decreases in the case of the Eu-doped sample, from 105(17) nm to 89(7) nm for Zn_2SnO_4 and Zn_2SnO_4:Eu samples, respectively, while their lattice microstrain is not significantly different, $2.90(11) \times 10^{-5}$ to $2.96(13) \times 10^{-5}$, respectively. This is in agreement with the results obtained from the SEM analysis, although the domain size obtained from the XRD is lower than the particle size as

DOI: 10.1021/acs.jpcc.6b05335
J. Phys. Chem. C 2016, 120, 18887−18894

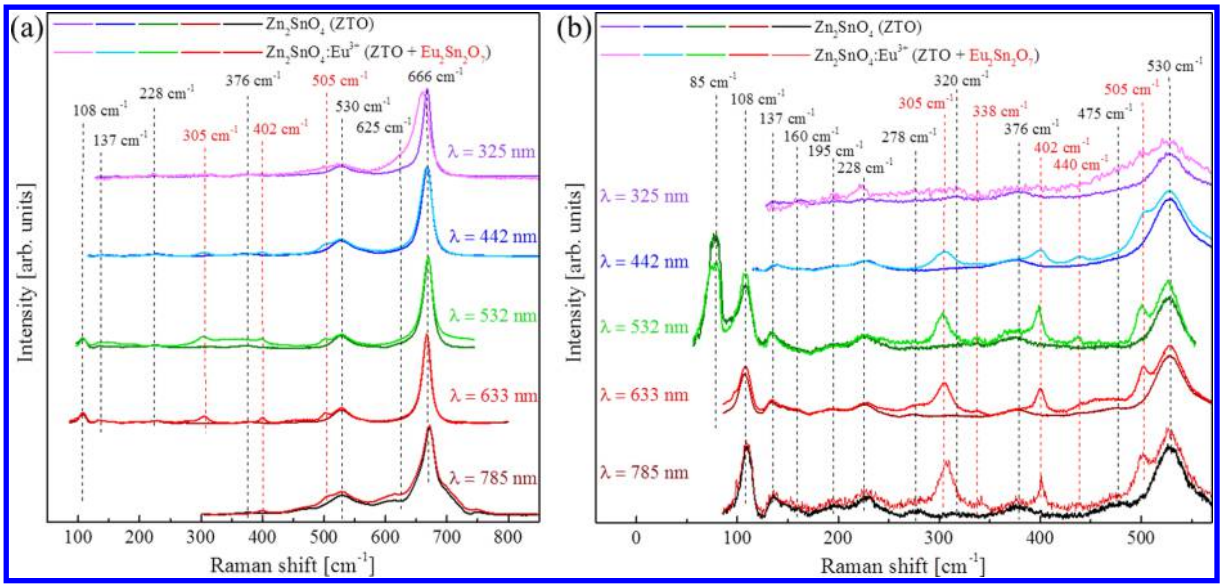

Figure 3. (a) Raman spectra of Zn_2SnO_4 and Zn_2SnO_4:Eu recorded with five different excitation energies (325,442, 532, 633, and 785 nm). (b) Low-frequency region in greater detail, with minor peaks identified. In both graphs, the peaks marked in red correspond to the $Eu_2Sn_2O_7$ secondary phase.

observed by SEM analysis because the coherent scattering domains do not necessarily correspond to particle size.

3.2. Raman Spectroscopy Characterization and Lattice Dynamics Calculations. In Mulliken notation, the irreducible representation of the Γ-point modes for the spinel-type zinc stannate structure[20−22] is given as

$$\Gamma = A_{1g} \oplus 2A_{2u} \oplus E_g \oplus 2E_u \oplus 2T_{2u} \oplus 3T_{2g} \oplus 5T_{1u} \oplus T_{1g}$$

Here, the A modes are nondegenerate, while the E modes are doubly degenerate, and the T modes are triply degenerate. According to the selection rules for this crystal symmetry, one T_{1u} mode corresponds to acoustic phonons; the remaining $4T_{1u}$ optical modes are infrared (IR) active; and A_{1g}, E_g, and $3T_{2g}$ modes are Raman active, while the rest are silent modes.

Figure 3 presents the Raman spectra of both Zn_2SnO_4 and Zn_2SnO_4:Eu powders measured with 325, 442, 532, 633, and 785 nm excitation wavelengths. Simultaneous fitting with Lorentzian curves of the Raman spectra measured with all excitations was performed, leading to identification of 18 experimentally observed peaks. Some of the peaks (305, 338, 402, 440, and 501 cm^{-1}) are attributed to the $Eu_2Sn_2O_7$ phase,[23,24] as already evidenced from SEM and XRD analysis.

To resolve and identify the other 13 peaks, density functional theory calculations were performed from which lattice vibrational mode frequencies were obtained. Figure 4 shows the phonon dispersion curves across the Brillouin zone for the spinel-type zinc stannate structure.

On the basis of the group theory analysis, Raman spectra of ideal Zn_2SnO_4 bulk crystals should be characterized with only five modes, which are predicted theoretically to be at 143, 227, 377, 532, and 667 cm^{-1} and which are assigned to $T_{2g}(1)$, E_g, $T_{2g}(2)$, $T_{2g}(3)$, and A_{1g} symmetries, respectively. These are in excellent agreement with experimentally observed peaks at 137, 228, 376, 530, and 666 cm^{-1} in the Raman spectra (the medium deviation of calculated mode frequencies from experimental values is only 1.1%) and with previously reported results.[2,25,26] According to the theoretical calculations, only the

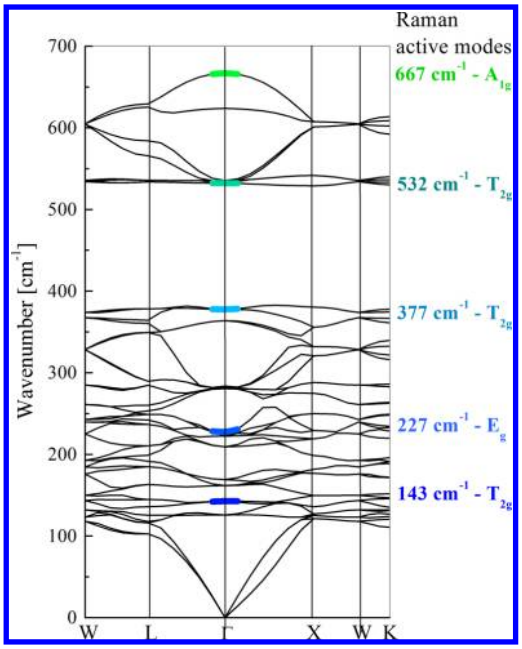

Figure 4. DFT-calculated phonon dispersion relations across the Brillouin zone of Zn_2SnO_4.

lowest frequency Raman mode involves motion of Sn (along with oxygen), while oxygen atoms are exclusively involved in other vibrations.

It is obvious from Figure 2 that, in addition to these five modes, eight other peaks are clearly observed in the Raman spectra. These peaks cannot be attributed to $Eu_2Sn_2O_7$ (peaks belonging to this phase have already been identified) or to any other secondary phases (EDX and XRD analyses have already excluded the presence of other secondary phases). These additional peaks correspond apparently to the IR and silent modes, which, strictly speaking, are forbidden by scattering selection rules for an ideal spinel-type crystal. Activation of the IR and silent modes in the Raman spectra could be associated with a disorder of the cation sublattice caused by the

DOI: 10.1021/acs.jpcc.6b05335
J. Phys. Chem. C 2016, 120, 18887−18894

mechanochemical synthesis method. It appears that a redistribution of cations over the tetrahedral and octahedral crystalline sites is responsible for a deviation of real structure from the ideal cubic inverse spinel. This is further confirmed by the fact that the experimental Raman spectra in the lower frequency region closely follow the calculated phonon density of states, as it is evident from Figure 5. Observation of phonon density of states (DOS) in Raman scattering spectra of disordered crystals is known experimentally.[27−29] Similarly, phonon confinement effects due to a reduction of crystallite size or to local (on the microscopic level) deviations of the structure from the global one are also known to cause the relaxation of the Raman scattering selection rules.[30−32]

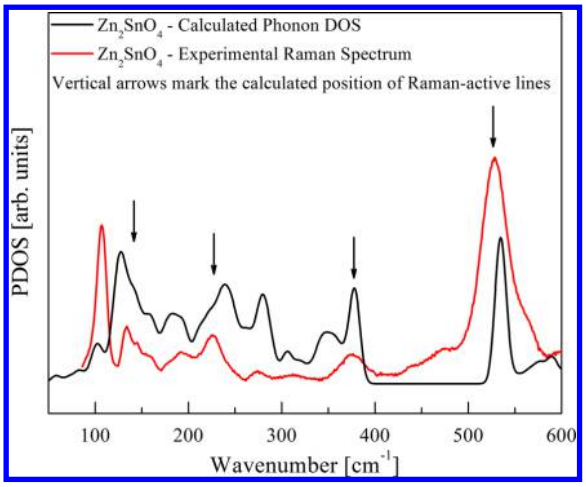

Figure 5. Comparison between the calculated phonon density of states and the experimental Raman spectra of Zn_2SnO_4 measured with 633 nm excitation. A notable overlap of the phonon density of states is observed in the lower frequency region of the Raman spectra, indicating the presence of a disordered structure.

Frequencies of all Raman peaks both experimentally observed and theoretically calculated and their proposed symmetry assignment are presented in Table 1. Table 1 also contains a comparison to the previously reported experimental data for Zn_2SnO_4 and $Eu_2Sn_2O_7$ compounds.[2,24−26]

3.3. Photoluminescence and Optical Band Gap Measurements. Further convincing experimental evidence for cation sublattice disorder comes from the analysis of the PL spectra of Zn_2SnO_4 and Zn_2SnO_4:Eu nanoparticles measured with 532 nm excitation and presented in Figure 6a.

The PL emission spectra of Zn_2SnO_4:Eu nanoparticles exhibit four sets of very intense bands in the 570−680 nm region. By comparing this spectrum with that of the Zn_2SnO_4 sample (i.e., without any Eu-doping, Figure 6a), which exhibits only a very broad low intensity emission with no visible peaks in this region, it is reasonable to assign these lines to transitions related to Eu^{3+} ions. The features centered at 580, 595, 615, and 655 nm are characteristic $^5D_0$-$^7F_0$, $^5D_0$-$^7F_1$, $^5D_0$-$^7F_2$, and $^5D_0$-$^7F_3$ emission bands of the Eu^{3+} ions, respectively.[33] Additionally, the relative intensities of the two orange emissions at 595 and 615 nm, which correspond to the magnetic ($^5D_0$-$^7F_1$) and electric dipole transitions ($^5D_0$-$^7F_2$), respectively, reflect the symmetry of the lattice sites occupied by Eu ions in the host structure. Depending on the symmetry of the occupancy site of

Table 1. Frequency (in cm^{-1}) of Peaks from Simultaneous Fitting of Raman Spectra Measured with 325, 442, 532, 632, and 785 nm Excitation Wavelengths of Zn_2SnO_4 and Zn_2SnO_4:Eu Compounds and Calculated from First-Principle Simulations for Zn_2SnO_4, Proposed Mode Symmetry Assignment, and Mode Activity[a]

this work									
Zn_2SnO_4				Zn_2SnO_4:Eu	reference for Zn_2SnO_4			reference for $Eu_2Sn_2O_7$	
ν_{exp} [cm^{-1}][b]	ν_{theo} [cm^{-1}][c]	sym[d]	mode activity	ν_{exp} [cm^{-1}][b]	ν [cm^{-1}][e]	ν [cm^{-1}][e]	ν [cm^{-1}][e]	ν [cm^{-1}][e]	sym[d]
85				85					
108	125.9	T_{2u}	silent	108		107			
137	142.7	T_{2g}	Raman	137			148		
160	161.7	T_{1u}	IR	160					
	169.0	E_u	silent						
195	209.3	T_{1g}	silent	195					
	222.4	T_{1u}	IR						
228	226.7	E_g	Raman	228		224	226		
278	280.5	T_{2u}	silent	278					
	281.9	T_{1u}	IR						
	283.5	A_{2u}	silent						
				305*				305	T_{2g}
				338*				339	E_g
320	363.8	E_u	silent	320					
376	377.4	T_{2g}	Raman	376	381		375		
				402*				399	T_{2g}
				440*					
475	535.3	T_{1u}	IR	475	467		435		
				501*				502	A_{1g}
530	532.2	T_{2g}	Raman	530	527	528	526		
625	623.7	A_{2u}	silent	625					
666	667.0	A_{1g}	Raman	666	667	668	667		

[a]For easer identifications, peaks attributed to the $Eu_2Sn_2O_7$ phase are marked with *. [b]Mode frequency obtained from the experiment. [c]Mode frequency obtained from the calculations. [d]Symmetry of modes. [e]Mode frequency obtained from refs 2 and 24−26.

DOI: 10.1021/acs.jpcc.6b05335
J. Phys. Chem. C 2016, 120, 18887−18894

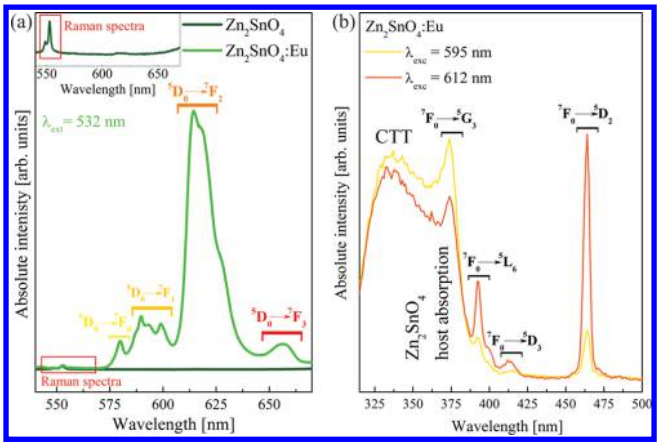

Figure 6. (a) PL spectra of Zn_2SnO_4 and Zn_2SnO_4:Eu nanoparticles measured under 532 nm excitation. Groups of lines correspond to transitions within different $^5D_0 - {}^7F_j$ (j = 0−3) multiplets, as labeled. (b) Excitation spectra of Zn_2SnO_4:Eu nanoparticles monitored at 595 nm (the transition of $^5D_0$-$^7F_1$) and at 612 nm (the transition of $^5D_0$-$^7F_2$). Groups of lines correspond to $^7F_0$-$^5G_3$, $^7F_0$-$^5L_6$, $^7F_0$-$^5D_3$, $^7F_0$-$^5D_2$ transitions, as labeled.

Eu^{3+} ion in the lattice, one of these transitions will dominate because of the different nature of these transitions.

According to the selection rules in Russell−Saunders coupling, electric dipole transitions are strictly spin- and parity-forbidden within the 4f configuration, whereas the magnetic dipole transitions are only spin-forbidden. However, the spin selection rule is partly lifted because of spin−orbit coupling, while the parity selection rules may be relaxed in crystals by mixing of levels of the 4f configuration with appropriate levels of configurations of opposite symmetry by way of odd terms in a static of dynamic crystal field expansion.[33] If Eu^{3+} ions occupy a lattice site with a strict center of symmetry, then the odd terms of the static crystal field vanish, leading to electric dipole transitions being strictly forbidden for purely electric transitions. On the other side, if Eu^{3+} ions occupy a noncentrosymmetric lattice site, then both the electric and magnetic transitions are possible. The first case will produce predominantly the 595 nm emission, while nonsymmetric site occupancy will lead to a dominant 615 nm emission.[33] The prevailing of the $^5D_0$-$^7F_2$ electric dipole transition at 615 nm over the $^5D_0$-$^7F_1$ magnetic dipole transition at 595 nm in the case of Zn_2SnO_4:Eu nanoparticles leads to the conclusion that the Eu^{3+} ions are generally located in a disordered surrounding in the Zn_2SnO_4 matrix.

The Eu^{3+} ions could occupy either the tetrahedral sites of Zn^{2+} or the octahedral sites of Sn^{4+} or Zn^{2+} in the Zn_2SnO_4 inverse spinel crystal structure. As a consequence of both these sites being centrosymmetric, electric dipole transitions ($^5D_0$-$^7F_{j=0,\,2}$) are forbidden and as such should not appear in the spectra. However, introduction of the Eu^{3+} ions in the Zn_2SnO_4 lattice will result in disorder and point defects in the lattice because of the differences in the ionic radius (Eu^{3+}/Sn^{4+} = 1.38 and Eu^{3+}/Zn^{2+} = 1.28) and the chemical valence. The charge compensating oxygen vacancies surrounding the Eu^{3+} ions will lead to the deviation from the point symmetry and relaxation of electric dipole transitions selection rules, with the appearance of the $^5D_0$-$^7F_{j=0,\,2}$ transition lines in the spectra. Additionally, the Eu^{3+} luminescent centers contributing to the $^5D_0$-$^7F_2$ transition line are probably located at the Zn_2SnO_4 particle surface or subsurface, where the crystal field is not as strong as at the lattice site. The observed excitation lines of Eu ions are generated from Eu ions situated in the Zn_2SnO_4 lattice, rather than from the Eu-rich $Eu_2Sn_2O_7$ phase, as the latter is known to greatly suppress the Eu emission.[34]

To distinguish how many different symmetry sites the Eu^{3+} ions occupy, excitation spectra monitored at 595 nm (the transition of $^5D_0$-$^7F_1$) and at 612 nm (the transition of $^5D_0$-$^7F_2$) were collected for the Zn_2SnO_4:Eu nanoparticles (Figure 6b). Both excitation spectra consist of a broad band and several narrow bands. The narrow bands at about 378, 395, 414, and 464 nm are attributed to the $^7F_0$-$^5G_3$, $^7F_0$-$^5L_6$, $^7F_0$-$^5D_3$, and $^7F_0$-$^5D_2$ transitions of the Eu^{3+} ions, respectively.[4,35−38] The broad band peaked at about 335 nm should be assigned to the overlap of the host absorption and the charge-transfer transition (CTT).[4,35−38] The host absorption represents transition between the valence band (derived mostly from O-2p with a minor contribution of Zn-3d states)[39] and the conduction band (formed mostly by the Zn-3p and 4s states (tetrahedral sites)),[39] while the CTT corresponds to the transition of the electron from the valence band to the Eu^{3+} localized state. Furthermore, the position of this broad peak in Figure 6b coincides well with the absorption band of pure Zn_2SnO_4, with an optical band gap of 3.35 eV (Figure S1 in Supporting Information), which indicates that the Eu^{3+} ions can be effectively excited through the Zn_2SnO_4 host lattice.

Similarity in the observed features of the excitation spectra monitored at different wavelengths suggests that the Eu^{3+} ions probably occupy only one lattice site. These results are further supported by measuring the decay times of the Eu^{3+} ions for emissions at 595 and 612 nm, under 464 nm excitation. The decay curves of the $^5D_0$-$^7F_1$ and $^5D_0$-$^7F_2$ transitions are presented in Figure S2. The lifetimes obtained after fitting with the double-exponential function have yielded values of 0.74(5) ms and 0.79(5) ms for the 595 and 612 nm emissions, respectively. Resemblance in the obtained lifetime values within the experimental uncertainty further points to the fact that the Eu^{3+} ions probably occupy only one lattice site. The differences in the decay curve traces are probably occurring because of the influence of Eu^{3+} luminescence centers which are located at the surface or subsurface of the Zn_2SnO_4 nanoparticles, as mentioned previously. Considering that the Zn^{2+} ions in tetrahedral sites are not replaced because of the large octahedral stabilization energy of Eu^{3+}, europium is assumed to be primarily located at the octahedral site of Sn^{4+} or Zn^{2+} under a weak crystal field. While all experimental results point to the incorporation of Eu^{3+} ions at only one lattice site, the possibility of existence of additional lattice sites cannot be excluded at this point. Detailed luminescence measurements on Eu-doped Zn_2SnO_4 single crystals should provide more comprehensive results about the incorporation of Eu^{3+} ions in different symmetry sites in the host lattice.

According to experimental data and the discussion presented earlier, a simplified energy level scheme for the Eu^{3+} ions and for the optical transitions observed in Figure 6 is indicated in Figure 7.

4. SUMMARY

To summarize, the phosphor activation of mechanochemically synthesized Zn_2SnO_4 nanoparticles with Eu is reported. XRD, Raman, and PL spectroscopies, as well as first principles lattice dynamics calculations, were utilized to characterize Zn_2SnO_4 and Zn_2SnO_4:Eu. The results show that Zn_2SnO_4 crystallizes in the cubic inverse spinel structure with space group $Fd\bar{3}m$ (O_h^7)

DOI: 10.1021/acs.jpcc.6b05335
J. Phys. Chem. C 2016, 120, 18887−18894

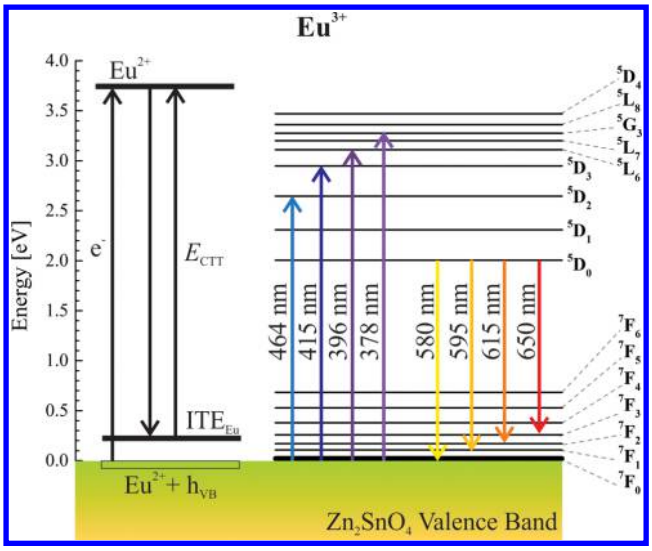

Figure 7. Energy-level scheme of Eu^{3+} ions with indication of the radiative transitions observed. After the charge-transfer transition (CTT), the system consists of a Eu^{2+} ion and a hole (h_{VB}) in the valence band. Coulomb interaction between the Eu^{2+} and h_{VB} will lead to formation of the bound states, which are labeled as impurity trapped exciton states (ITE_{Eu}), and are located over the top of the valence band.[40]

and suggest that Eu^{3+} ions incorporate in limited quantities into the host nanocrystalline matrix. The formation of a secondary $Eu_2Sn_2O_7$ phase could also occur. Eu^{3+} is shown to occupy noncentrosymmetric sites in the Zn_2SnO_4 lattice. Excitation spectra and lifetime measurements suggest that Eu^{3+} ions are incorporated at only one symmetry site. According to the crystal field theory, it is assumed that Eu^{3+} ions participate at octahedral sites of Zn^{2+} or Sn^{4+} under a weak crystal field, rather than the tetrahedral sites of Zn^{2+}, because of the high octahedral stabilization energy for Eu^{3+}. The spinel-type Zn_2SnO_4 shows effectiveness in hosting Eu^{3+} ions, which could be used as a prospective green/red emitter.

■ ASSOCIATED CONTENT

Supporting Information

The Supporting Information is available free of charge on the ACS Publications website at DOI: 10.1021/acs.jpcc.6b05335.

Diffuse reflectance spectra, luminescence decay curves, and fitted curves of Zn_2SnO_4:Eu nanoparticles (PDF)

■ AUTHOR INFORMATION

Corresponding Author

*E-mail: mira.dimitrievska@gmail.com; mirjana.dimitrievska@nist.gov; mirjana.dimitrievska@nrel.gov. Phone: +1 (301) 975-0403.

Notes

The authors declare no competing financial interest.

■ ACKNOWLEDGMENTS

This work was supported by APV Provincial Secretariat for Higher Education and Scientific Research, and we acknowledge the support of the Ministry of Education, Science, and Technological Development of the Republic of Serbia (Project numbers: ON 171022 and III 45020) and the People Programme (Marie Curie Actions) of the European Union's Seventh Framework Programme FP7/2007−2013/under REA grant agreement n°316488 (KESTCELLS). A. P. L. acknowledges the support from the State of Texas though the TcSUH at the University of Houston. M. D. gratefully acknowledges research support from the U.S. Department of Energy, Office of Energy Efficiency and Renewable Energy, Fuel Cell Technologies Office, under Contract No. DE-AC36-08GO28308. The authors would like to thank Dr. Miroslav Dramicanin (Vinča Institute of Nuclear Sciences, Belgrade, Serbia) for the luminescence measurements and productive discussions.

■ REFERENCES

(1) Baruah, S.; Dutta, J. Zinc Stannate Nanostructures: Hydrothermal Synthesis. *Sci. Technol. Adv. Mater.* **2011**, *12* (1), 13004.

(2) Šepelák, V.; Becker, S. M.; Bergmann, I.; Indris, S.; Scheuermann, M.; Feldhoff, A.; Kübel, C.; Bruns, M.; Stürzl, N.; Ulrich, A. S.; et al. Nonequilibrium Structure of Zn_2SnO_4 Spinel Nanoparticles. *J. Mater. Chem.* **2012**, *22* (7), 3117−3126.

(3) Yang, C.-C.; Cheng, S.-Y.; Lee, H.-Y.; Chen, S.-Y. Effects of Phase Transformation on Photoluminescence Behavior of ZnO:Eu Prepared in Different Solvents. *Ceram. Int.* **2006**, *32* (1), 37−41.

(4) Fu, Z.; Yang, H. K.; Moon, B. K.; Choi, B. C.; Jeong, J. H. Hydrothermal Synthesis and Optical Characteristics of Eu^{3+} in Zn_2SnO_4 Nanocrystals. *Curr. Appl. Phys.* **2009**, *9* (6), 1360−1364.

(5) Chen, Y.-C.; Chang, Y.-H.; Tsai, B.-S. Photoluminescent Properties of Europium-Activated Zn_2SnO_4 Phosphors. *Mater. Trans.* **2004**, *45* (5), 1684−1686.

(6) Xie, H.; Lu, J.; Guan, Y.; Huang, Y.; Wei, D.; Seo, H. J. Abnormal Reduction, $Eu^{3+} \rightarrow Eu^{2+}$, and Defect Centers in Eu^{3+}-Doped Pollucite, $CsAlSi_2O_6$, Prepared in an Oxidizing Atmosphere. *Inorg. Chem.* **2014**, *53* (2), 827−834.

(7) Baran, A.; Mahlik, S.; Grinberg, M.; Zych, E. High Pressure and Time-Resolved Luminescence Spectra of $Ca_3Y_2(SiO_4)_3$ Doped with Eu^{2+} and Eu^{3+}. *J. Phys.: Condens. Matter* **2013**, *25* (2), 25603.

(8) Šepelák, V.; Düvel, A.; Wilkening, M.; Becker, K.-D.; Heitjans, P. Mechanochemical Reactions and Syntheses of Oxides. *Chem. Soc. Rev.* **2013**, *42* (18), 7507−7520.

(9) The mention of all commercial suppliers in this paper is for clarity. This does not imply the recommendation or endorsement of these suppliers by NIST.

(10) Ivetić, T. B.; Finčur, N. L.; Đačanin, L. R.; Abramović, B. F.; Lukić-Petrović, S. R. Ternary and Coupled Binary Zinc Tin Oxide Nanopowders: Synthesis, Characterization, and Potential Application in Photocatalytic Processes. *Mater. Res. Bull.* **2015**, *62*, 114−121.

(11) Dimitrievska, M.; Fairbrother, A.; Fontané, X.; Jawhari, T.; Izquierdo-Roca, V.; Saucedo, E.; Pérez-Rodríguez, A. Multiwavelength Excitation Raman Scattering Study of Polycrystalline Kesterite Cu_2ZnSnS_4 Thin Films. *Appl. Phys. Lett.* **2014**, *104* (2), 21901.

(12) Dimitrievska, M.; Xie, H.; Fairbrother, A.; Fontané, X.; Gurieva, G.; Saucedo, E.; Pérez-Rodríguez, A.; Schorr, S.; Izquierdo-Roca, V. Multiwavelength Excitation Raman Scattering of $Cu_2ZnSn(S_xSe_{1-x})_4$ ($0 \leq X \leq 1$) Polycrystalline Thin Films: Vibrational Properties of Sulfoselenide Solid Solutions. *Appl. Phys. Lett.* **2014**, *105* (3), 31913.

(13) Perdew, J. P.; Burke, K.; Ernzerhof, M. Generalized Gradient Approximation Made Simple. *Phys. Rev. Lett.* **1996**, *77* (18), 3865−3868.

(14) Clark, S. J.; Segall, M. D.; Pickard, C. J.; Hasnip, P. J.; Probert, M. I. J.; Refson, K.; Payne, M. C. First Principles Methods Using CASTEP. *Z. Kristallogr. - Cryst. Mater.* **2005**, *220* (5/6), 567−570.

(15) Monkhorst, H. J.; Pack, J. D. Special Points for Brillouin-Zone Integrations. *Phys. Rev. B* **1976**, *13* (12), 5188−5192.

(16) Momma, K.; Izumi, F. *VESTA 3* for Three-Dimensional Visualization of Crystal, Volumetric and Morphology Data. *J. Appl. Crystallogr.* **2011**, *44* (6), 1272−1276.

(17) Segev, D.; Wei, S.-H. Structure-Derived Electronic and Optical Properties of Transparent Conducting Oxides. *Phys. Rev. B: Condens. Matter Mater. Phys.* **2005**, *71* (12), 125129.

DOI: 10.1021/acs.jpcc.6b05335
J. Phys. Chem. C 2016, 120, 18887−18894

(18) Williamson, G. K.; Hall, W. H. X-Ray Line Broadening from Filed Aluminium and Wolfram. *Acta Metall.* **1953**, *1* (1), 22−31.
(19) Mote, V. D.; Purushotham, Y.; Dole, B. N. Williamson-Hall Analysis in Estimation of Lattice Strain in Nanometer-Sized ZnO Particles. *J. Theor. Appl. Phys.* **2012**, *6* (1), 1−8.
(20) Aroyo, M. I.; Kirov, A.; Capillas, C.; Perez-Mato, J. M.; Wondratschek, H. Bilbao Crystallographic Server. II. Representations of Crystallographic Point Groups and Space Groups. *Acta Crystallogr., Sect. A: Found. Crystallogr.* **2006**, *62* (2), 115−128.
(21) Aroyo, M. I.; Perez-Mato, J. M.; Capillas, C.; Kroumova, E.; Ivantchev, S.; Madariaga, G.; Kirov, A.; Wondratschek, H. Bilbao Crystallographic Server: I. Databases and Crystallographic Computing Programs. *Z. Kristallogr. - Cryst. Mater.* **2009**, *221* (1), 15−27.
(22) Aroyo, M. I.; Perez-Mato, J. M.; Orobengoa, D.; Tasci, E.; De La Flor, G.; Kirov, A. Crystallography Online: Bilbao Crystallographic Server. *Bulg. Chem. Commun.* **2011**, *43* (2), 183−97.
(23) Hirano, M.; Ohmori, T. Direct Formation and Luminescence of Nanocrystals in the System $Eu_2Sn_2O_7$−$Gd_2Sn_2O_7$ Complete Solid Solutions. *J. Am. Ceram. Soc.* **2015**, *98* (12), 3726−3732.
(24) Zhang, J.; Zhang, A.; Tie, X.; Cui, N. Hydrothermal Synthesis and Photocatalytic Activities Characterization of Europium (III) Stannate. *J. Mol. Catal.* **2008**, *6*, 11.
(25) Wang, J. X.; Xie, S. S.; Yuan, H. J.; Yan, X. Q.; Liu, D. F.; Gao, Y.; Zhou, Z. P.; Song, L.; Liu, L. F.; Zhao, X. W.; et al. Synthesis, Structure, and Photoluminescence of Zn_2SnO_4 Single-Crystal Nanobelts and Nanorings. *Solid State Commun.* **2004**, *131* (7), 435−440.
(26) Nikolić, M. V.; Ivetić, T.; Young, D. L.; Paraskevopoulos, K. M.; Zorba, T. T.; Blagojević, V.; Nikolić, P. M.; Vasiljević-Radović, D.; Ristić, M. M. Far Infrared Properties of Bulk Sintered and Thin Film Zn2SnO4. *Mater. Sci. Eng., B* **2007**, *138* (1), 7−11.
(27) Paudel, T. R.; Lambrecht, W. R. L. Calculated Phonon Band Structure and Density of States and Interpretation of the Raman Spectrum in Rocksalt ScN. *Phys. Rev. B: Condens. Matter Mater. Phys.* **2009**, *79* (8), 85205.
(28) Spengler, W.; Kaiser, R.; Christensen, A. N.; Müller-Vogt, G. Raman Scattering, Superconductivity, and Phonon Density of States of Stoichiometric and Nonstoichiometric TiN. *Phys. Rev. B: Condens. Matter Mater. Phys.* **1978**, *17* (3), 1095−1101.
(29) Spengler, W.; Kaiser, R. First and Second Order Raman Scattering in Transition Metal Compounds. *Solid State Commun.* **1976**, *18* (7), 881−884.
(30) Placidi, M.; Dimitrievska, M.; Izquierdo-Roca, V.; Fontané, X.; Castellanos-Gomez, A.; Pérez-Tomás, A.; Mestres, N.; Espindola-Rodriguez, M.; López-Marino, S.; Neuschitzer, M.; et al. Multi-wavelength Excitation Raman Scattering Analysis of Bulk and Two-Dimensional MoS_2: Vibrational Properties of Atomically Thin MoS2 Layers. *2D Mater.* **2015**, *2* (3), 35006.
(31) Ivanov, V. G.; Abrashev, M. V.; Iliev, M. N.; Gospodinov, M. M.; Meen, J.; Aroyo, M. I. Short-Range B-Site Ordering in Inverse Spinel Ferrite $NiFe_2O_4$. *Phys. Rev. B: Condens. Matter Mater. Phys.* **2010**, *82*, 2.
(32) Dimitrievska, M.; Fairbrother, A.; Pérez-Rodríguez, A.; Saucedo, E.; Izquierdo-Roca, V. Raman Scattering Crystalline Assessment of Polycrystalline Cu_2ZnSnS_4 Thin Films for Sustainable Photovoltaic Technologies: Phonon Confinement Model. *Acta Mater.* **2014**, *70*, 272−280.
(33) Blasse, G.; Bril, A.; Nieuwpoort, W. C. On the Eu^{3+} Fluorescence in Mixed Metal Oxides. *J. Phys. Chem. Solids* **1966**, *27* (10), 1587−1592.
(34) Bazargan, S.; Leung, K. T. Nano-Environment Effects on the Luminescence Properties of Eu^{3+}-Doped Nanocrystalline SnO_2 Thin Films. *J. Chem. Phys.* **2012**, *137* (18), 184704.
(35) Lin, L.; Sun, X.; Jiang, Y.; He, Y. Sol-Hydrothermal Synthesis and Optical Properties of Eu^{3+}, Tb^{3+}-Codoped One-Dimensional Strontium Germanate Full Color Nano-Phosphors. *Nanoscale* **2013**, *5* (24), 12518−12531.
(36) Li, J.-G.; Wang, X.; Watanabe, K.; Ishigaki, T. Phase Structure and Luminescence Properties of Eu^{3+}-Doped TiO_2 Nanocrystals Synthesized by Ar/O_2 Radio Frequency Thermal Plasma Oxidation of Liquid Precursor Mists. *J. Phys. Chem. B* **2006**, *110* (3), 1121−1127.
(37) You, H.; Nogami, M. Local Structure and Persistent Spectral Hole Burning of the Eu^{3+} Ion in SnO_2−SiO_2 Glass Containing SnO_2 Nanocrystals. *J. Appl. Phys.* **2004**, *95* (5), 2781−2785.
(38) Behrendt, M.; Mahlik, S.; Szczodrowski, K.; Kuklinski, B.; Grinberg, M. Spectroscopic Properties and Location of the Tb^{3+} and Eu^{3+} Energy Levels in Y_2O_2S under High Hydrostatic Pressure. *Phys. Chem. Chem. Phys.* **2016**, DOI: 10.1039/C6CP03075K.
(39) Recio, J. M.; Menendez, J. M.; Roza, A. O. de la. *An Introduction to High-Pressure Science and Technology*; CRC Press: Boca Raton, FL, USA, 2016.
(40) Grinberg, M. Excited States Dynamics under High Pressure in Lanthanide-Doped Solids. *J. Lumin.* **2011**, *131* (3), 433−437.

DOI: 10.1021/acs.jpcc.6b05335
J. Phys. Chem. C 2016, 120, 18887−18894